

Spectral Evolution of The Parsec-Scale Jet in The Quasar 3C 345

Andrew P. Lobanov^{1,2} and J. Anton Zensus^{1,2}

Received _____; accepted _____

arXiv:astro-ph/9903318v1 22 Mar 1999

¹Max-Planck-Institut für Radioastronomie, Auf dem Hügel 69, Bonn 53121, Germany.
E-mail: alobanov@mpifr-bonn.mpg.de, azensus@mpifr-bonn.mpg.de

²National Radio Astronomy Observatory, 520 Edgemont Rd., Charlottesville, VA 22903, USA

ABSTRACT

The long-term evolution of the synchrotron emission from the parsec-scale jet in the quasar 3C 345 is analysed, on the basis of multi-frequency monitoring with very long baseline interferometry (VLBI) and covering the period 1979–1994. We demonstrate that the compact radio structure of 3C 345 can be adequately represented by Gaussian model fits and that the model fits at different frequencies are sufficiently reliable for studying the spectral properties of the jet. We combine the model fits from 44 VLBI observations of 3C 345 made at 8 different frequencies between 2.3 and 100 GHz. This combined database is used for deriving the basic properties of the synchrotron spectra of the VLBI core and the moving features observed in the jet. We calculate the turnover frequency, turnover flux density, integrated 4–25 GHz flux and 4–25 GHz luminosity of the core and the moving features. The core has an estimated mean luminosity $L_{\text{core}} = (7.1 \pm 3.5) \cdot 10^{42} h^{-2} \text{ erg s}^{-1}$; the estimated total luminosity of 3C 345 on parsec scales is $\approx 3 \cdot 10^{43} h^{-2} \text{ erg s}^{-1}$ (about 1% of the observed luminosity of the source between the radio to infrared regimes). The luminosities of the core and most of the moving features decrease at the average rate of $1.2 \cdot 10^{35} h^{-2} (0.74 \pm 0.06)^{t-1979.0} \text{ erg s}^{-2}$ (t measured in years). The derived luminosity variations require intrinsic acceleration of the moving features. The turnover frequency of one of the moving features reaches a peak during the above period. The combination of the overall spectral and kinematic changes in that feature cannot be reproduced satisfactorily by relativistic shocks, which may indicate rapid dissipation in shocks. The spectral changes in the core can be reconciled with a shock or dense plasma condensation traveling through the region where the jet becomes optically thin. We are able to describe the evolution of the core spectrum by a sequence of 5 flare-like events characterized by an exponential rise and decay of the particle number density of the material injected into the jet. The same model is also capable of predicting the changes in the flux density observed in the core. The flares occur approximately every 3.5–4 years, roughly correlating with appearances of new moving features in the jet, and indicating that a quasi-periodic process in the nucleus may be driving the observed emission and structural evolution of 3C 345.

Subject headings: radiative mechanisms: non-thermal — methods: data analysis — galaxies: jets — quasars: individual (3C 345) — radio continuum: galaxies

1. Introduction

The 16^m quasar 3C 345 ($z = 0.595$, Hewitt & Burbidge 1993) is one of the best examples of an active galactic nucleus (AGN) showing structural and flux variability on parsec scales around a compact unresolved radio core (for comprehensive reviews, see Zensus, Krichbaum, & Lobanov 1995, and Zensus 1997). The source has been detected in all wave bands except for γ -ray ($E > 100$ MeV) where only an upper limit of the flux is known (Fichtel et al. 1994). In the X-ray regime, the source is weak and possibly variable (Halpern 1982; Makino 1989; Worrall and Wilkes 1990). At 1 keV, the flux density is $S_x = 0.39 \pm 0.03$ mJy. The spectral index is $\alpha_x \approx -0.9$ in the 0.2–2.0 keV spectral band (Unwin et al. 1994). In the ultraviolet, the flux density is $S_{uv} \approx 6$ mJy, assuming a column density of neutral hydrogen $N_H = 10^{20}$ cm⁻² and a spectral slope similar to that of the X-ray emission (Malina et al. 1994). In the optical regime, the source is highly polarized (Moore & Stockman 1984) and variable. The observed variations are possibly quasi-periodic with a period of ≈ 1560 days (Babadzhanyants and Belokon’ 1984; Kidger 1990), although it has been suggested that the light curve may originate from a non-linear and non-stationary stochastic process (Vio et al. 1990). Infrared observations of 3C 345 show $S_{60\mu\text{m}} \approx 0.7$ Jy (Impey & Neugebauer 1988).

The total radio flux density of 3C 345 has been monitored at 5, 8, and 15 GHz (Aller, Aller, & Hughes 1996), and at 22 and 37 GHz (Teräsraanta et al. 1998). The source has also been monitored with the Green Bank Interferometer at 2.7 and 8.1 GHz (Waltman et al. 1991). The continuum radio spectrum is flat up to 10 GHz, and steepens towards higher frequencies, with the spectral index ranging from -0.9 to -1.4 . (Bregman et al. 1986). The time scale of the variability shortens towards higher frequencies, suggesting the presence of at least two emitting regions in the source core (Bregman et al. 1986).

VLA observations of 3C 345 (Kollgaard et al. 1989) show a faint halo around a bright core, and an extended kiloparsec-scale jet. On smaller scales, the source structure is predominantly of core-jet type. The parsec-scale emission of 3C 345 has been monitored extensively with very long baseline interferometry (VLBI) (Unwin et al., 1983; Biretta, Moore & Cohen 1986, hereafter BMC86; Zensus, Cohen, & Unwin 1995, hereafter ZCU95). The monitoring has been performed at 5, 8.4, 10.7, and 22.3 GHz, and additional observations have been made at 2.3, 43, 89, and 100 GHz. Recent VLBI observations covering the epochs between 1989 and 1997 are presented in Lobanov (1996, hereafter L96) and Ros et. al (1999).

The relativistic jet model (Blandford & Rees 1978) has been applied to 3C 345 to explain the nature of the enhanced emission regions in the jet. Using the X-ray data to constrain the jet kinematics, ZCU95 and Unwin et al. (1994) have derived the physical conditions of the jet from a model that combines the inhomogeneous-jet model of Königl (1981) for the core with homogeneous synchrotron spheres for the jet components (Cohen 1985). Unwin et al. (1997) have analysed a correlation between the X-ray variability and parsec-scale radio structure of 3C 345. Steffen et al. (1995) derived a helical jet model

to explain the observed component trajectories and flux density variations. Rabaça and Zensus (1994) showed that the flux evolution of the jet component C4 is consistent with a strong shock concentrated in a narrow region. Wardle et al. (1994) have shown that the polarization structure can also be reproduced within the relativistic shock model.

Because of the limitations of VLBI observations, spectral properties and spectral variations of parsec-scale emission have so far not been studied in detail. Such a study requires a homogeneous VLB array, reliable amplitude calibrations, quasi-simultaneous observations at different frequencies, and analysing the emission at different frequencies continuously along the jet. For two recent epochs, the turnover frequency distributions in 3C 345 and 3C 273 have been mapped and the magnetic field profiles have been obtained in (Lobanov & Zensus 1994, Lobanov, Carrara, & Zensus 1997, Lobanov 1998b). Owing to the insufficient data quality, it is not possible to extend this analysis to earlier observations; we must therefore resort to a simpler approach, combining observations made at nearby epochs, and using model fits to represent the source structure. At this time, this is the only plausible means to study, albeit crudely, the long-term spectral evolution of parsec-scale radio emission.

In this paper, we use the available multi-frequency VLBI results to study the spectral evolution of different regions in the jet of 3C 345. In section 2, we give a summary of the VLBI data, and describe the procedures used for data analysis. We calculate the parameters of simple synchrotron spectra: the turnover frequency ν_m , the turnover flux density S_m , and the integrated 4–25 GHz flux S_{int} . The evolution of the spectrum and luminosity evolution of the jet are discussed in section 3. In section 4, the observed spectral changes in the moving features of the jet are compared with the predictions of the shock-in-jet model. In section 5, the observed variations of the spectrum and flux density of the VLBI core are modeled by flare-like events developing in an inhomogeneous jet.

Throughout this paper, we use the positive definition of spectral index, α ($S \propto \nu^\alpha$), a Hubble constant, $H_0 = 100 h \text{ km s}^{-1} \text{ Mpc}^{-1}$, and a deceleration parameter, $q_0 = 0.5$.

2. Multi-frequency VLBI data

We use data from 44 VLBI observations of 3C 345 made at 2.3, 5, 8.4, 10.7, 22.3, 43.2, 89.2, and 100 GHz during the period 1979.25–1993.88 (see Table 1 for references). Standard VLBI analysis was applied to all the data, with CLEAN δ -components used for representing the source structure (see Zensus, Diamond, & Napier 1995 for the most recent treatment of the subject). It is, however, very difficult to employ the CLEAN components for describing the kinematic and emission properties of VLBI-scale regions. We have therefore resorted to working with simple models of Gaussian or spherical components fitted directly to the interferometric visibility data. The models for earlier epochs (1979–1984) were taken from the literature; the models for later epochs have been made from the original data. We used

the MODELFIT routine of the Caltech VLBI package (Pearson 1991) and fitted the complex baseline visibilities using the maximum likelihood method (minimizing χ^2 , the weighted sum of squares of the deviations between the data and the model). We evaluated the goodness of the fit by the reduced chi-square, $\chi^2/(N_{\text{datapoints}} - N_{\text{parameters}})$, and determined the uncertainties of the fitted parameters from the corresponding confidence limits in the χ^2 distribution. This allowed us to account for increased uncertainties in cases when some of the fitted parameters could not be considered strictly independent (for instance, if the separation between two Gaussian components is smaller than their sizes; see Pearson 1995 for an extensive discussion of the model fitting technique). This model fitting technique has been shown to be a reliable tool for representing the VLBI-scale structure and emission in many sources, including 3C 345 itself (ZCU95) and even more complex sources, such as Cygnus A (Krichbaum et al. 1998).

EDITOR: PLACE FIGURE 1 HERE.

2.1. Model fitting the source structure in 3C 345

A VLBI image of 3C 345 at 8.4 GHz obtained from an observation made in November 1993 is shown on the top in Figure 1. The bottom image in Figure 1 is obtained by modeling the visibility data with 8 elliptical Gaussian components (the 8th component corresponds to a weak, distant feature C1 lying outside the plotted ranges). One can see the remarkable similarity between the VLBI image and the model fit representation of the source structure. This is also illustrated in Figure 2, where we compare the representations of the visibility amplitudes and closure phases by the model from CLEAN components and that from Gaussian components. The two representations are barely distinguishable only by the more rapid variations visible in the CLEAN component model (because of a wider area of the image plane used for determining the CLEAN component model). It is also remarkable that the exclusion of either C6 or C7 from the Gaussian model deteriorates the fit so much that it becomes impossible to achieve a satisfactory agreement with the data, no matter what adjustments are made to the remaining components. The presence of C6 and C7 in the jet is also self-evident in the VLBI image of 3C 345 made at a close epoch at 22 GHz, with a resolution about 3 times better (L96). This and numerous other examples of model fitting 3C 345 convince us of the suitability of Gaussian component models for describing the structure and emission in 3C 345.

In 3C 345, the VLBI core, D, is probably stationary (Tang et al. 1990), and the bright components C2–C7 embedded in the jet are receding from the core at apparent speeds ranging from 1 to 20c (ZCU95, L96). We limit our present discussion to the core D and the components C2–C5 which were dominating the source emission in the period 1979–1993. We obtain spectra and luminosities for D, C5, and C4, and only make luminosity estimates

for C2 and C3. Owing to the decreasing surface brightness of the extended jet, some of the recent measurements for the oldest feature C2 are not reliable. At distances larger than ≈ 5 mas, the emission regions in the jet tend to become more complicated, and generally more difficult to describe by a single Gaussian component. However, the bulk of the data that we use for our spectral fitting is related to the features of the jet at distances smaller than 5 mas, where the Gaussian representation is sufficient.

EDITOR: PLACE FIGURE 2 HERE.

2.2. Multi-frequency datasets

The VLBI observations at different frequencies were typically not made simultaneously; and we combine only those observing epochs which are sufficiently close in time, so that the source variability will not undermine the results. The light curves for the total and component flux densities yield time intervals of up to 6 months, during which the changes do not exceed the typical errors inherited from the model fitting. We use this limit to combine the flux data into multi-frequency datasets. A stricter limitation would result in too few possibilities of constructing such sets.

The multi-frequency datasets are listed in Table 1. Each set, except for the first two, contains observations at three or more frequencies. In all datasets, the lowest frequency is 5 GHz or lower. If a component is detected only at two frequencies within a given set, only the limiting values can be determined for the fitted spectral parameters.

EDITOR: PLACE TABLE 1 HERE.

2.3. Spectral fitting

We assume that spectrum of a jet component is similar to that of a homogeneous relativistic plasma with a power-law electron energy distribution

$$S_\nu \propto \left(\frac{\nu}{\nu_1}\right)^{5/2} \left\{ 1 - \exp \left[- \left(\frac{\nu_1}{\nu}\right)^{5/2-\alpha} \right] \right\} \quad (1)$$

(Pacholczyk 1970), where ν_1 is the frequency at which the optical depth is $\tau = 1$, and α is the spectral index. Instead of ν_1 , we use the frequency of spectral maximum ν_m (the turnover frequency). The two can be related, using a simple approximation $\nu_1 \approx 0.912(-\alpha)^{0.386}\nu_m$.

Since VLBI observations cover a relatively narrow spectral interval, ν_m may lie outside the observed frequency range. For such ill-constrained cases, we first fit the spectral data by polynomial functions, and then analyse local curvature of the fits obtained. We compare the value of the curvature obtained with the theoretical curvature of the synchrotron spectrum, and make an estimate (often only an upper limit) of ν_m . A detailed discussion of the procedure is given in Lobanov (1998b). The main steps of spectral fitting can be summarized as follows:

1) We make an approximate estimate of relevant frequency range, (ν_L, ν_H) , outside which the flux density level is negligibly small. For that purpose, we use the average measured turnover frequency and the spectral spectral index in the compact source. On the basis of these values, we estimate the frequencies ν_L and ν_H at which the corresponding flux density is at an arbitrarily low level (we use $S_{\text{cutoff}} = 0.1 \text{ mJy}$). Let us stress here that no specific physical meaning is attached to these quantities. We add these spectral points to the measured data solely for the purpose of ensuring a negative curvature of the fitted polynomial curves, as required by the theoretical spectral form (1). To account for possible uncertainties in the estimated values, we allow 15% variations of ν_L and ν_H , during each iterative cycle of the fitting routine described below.

In our estimates of ν_L and ν_H , we profit from the sharpness of the transition between the high-frequency ($\nu > \nu_1$) and low-frequency ($\nu < \nu_1$) spectral regimes determined by equation 1. The resulting spectrum is determined by the synchrotron self-absorption at frequencies $\nu \ll \nu_1$, and by the electron energy distribution at $\nu \gg \nu_1$. Estimates of the typical turnover frequency and energy spectral index in the jet of 3C345 based on our own calculations and on the results from Rabaça and Zensus (1994) give $\nu_1 \approx 10 \text{ GHz}$ and $\alpha \approx -0.7$. Using these values, we calculate the low-frequency, $\nu_L \sim 1 \text{ MHz}$, and high-frequency, $\nu_H \sim 1000 \text{ GHz}$, fiducial spectral points at which the flux density level is about 0.1 mJy , and use these values as the initial guesses for the spectral fitting.

2) We fit, iteratively, the combined spectrum by polynomial functions, allowing for limited variations of ν_L and ν_H , and aiming at achieving the best fit to the measured data points. From the fits, we obtain the initial estimates of the basic parameters of the spectra: the turnover frequency, ν_m , turnover flux density, S_m , and the integrated flux, S_{int} (the integration limits are set to a range of 4–25 GHz, the typical range of the observing frequencies).

3. The initial estimates of ν_m are corrected and classified as values or limits, by considering the local curvature of the fitted polynomial forms, and deriving the ranges of reliable corrections from the mean flux density errors in the multi-frequency datasets. We calculate the local curvature of the fitted spectra within the range of observing frequencies. The derived curvature can be compared with the values obtained from analytical or numerical calculations of the synchrotron spectrum. In this paper, we derive the corrected value of the turnover frequency, by equating the fitted and the theoretical

spectral curvatures.

4. We then fit the data with the synchrotron spectral form described by (1), using the corrected value of the turnover frequency, and obtaining the final estimates of S_m and S_{int} (the differences between the initial and final estimates of S_{int} are insignificant, since, by virtue of the fitting procedure applied, both the polynomial and synchrotron spectral forms are optimized to provide the best fit within the range of observing frequencies, which covers, in most cases, the range of 4–25 GHz used for calculating S_m). We obtain the formal errors of the fitted spectral parameters from Monte Carlo simulations, assuming Gaussian distribution of VLBI flux density errors, and analysing the distributions of the χ^2 parameters of the fits to the simulated datasets.

EDITOR: PLACE FIGURE 3 HERE.

2.3.1. Curvature of the fits

Here, we outline the application of the local curvature of the fitted polynomial forms to correcting and classifying the initial estimates of the spectral parameters. Following Apostol (1969), the local curvature, κ , of spectral fits, $S(\nu)$, can be written as:

$$\kappa = \frac{d^2S}{d\nu^2} \left[1 + \left(\frac{dS}{d\nu} \right)^2 \right]^{-1/3}. \quad (2)$$

If the spectral index, α_o , and the local curvature, κ_o , of a polynomial fit are determined at a frequency ν_o , then the turnover frequency, ν_m , can be estimated from the adopted theoretical synchrotron spectrum. Using the derived α_o and κ_o , we determine the ratio $\xi(\alpha_o, \kappa_o) = \nu_m/\nu_o$, from the adopted spectral form described by (1). The corresponding turnover frequency is then

$$\nu_m = \nu_o \xi(\alpha_o, \kappa_o). \quad (3)$$

Figure 3 relates the curvature κ of the homogeneous synchrotron spectrum to the ratio $\xi(\alpha_o, \kappa_o)$. For frequencies increasingly deviating from the turnover frequency, κ becomes progressively smaller, thereby limiting the ranges of applicability of the corrections described by (3). For data covering the frequencies from ν_l to ν_h , and for negligible ($\leq 1\%$) flux density errors, we expect the corrections to give reliable estimates for the turnover frequencies lying within the range of $0.05\nu_l < \nu_m < 2\nu_h$. For a spectral dataset containing N measured flux densities, $S_{\nu,i}$, and flux density errors, σ_i , we can estimate the minimum measurable curvature, κ_{min} , warranted by the data. We use the average fractional flux density error, $\sigma_{S,N} = \langle \sigma_i/S_{\nu,i} \rangle$, and obtain

$$\kappa_{\text{min}} = 2\hat{\sigma}[1 + (\alpha + 2\hat{\sigma}\nu_{h,l})^2]^{-1/3}, \quad (4)$$

where $\hat{\sigma} = \log(1 - \sigma_{S,N})$ and $\nu_{h,l} = \log(\nu_h)/\log(\nu_l)$. In Figure 3, we mark the ranges of $\xi(\alpha, \kappa)$ corresponding to κ_{\min} estimated for spectral datasets with average fractional flux density errors $\sigma_{S,N} = 1, 5, 10,$ and 20% . The $\sigma_{S,N}$ of our spectral datasets are given in the 4th column of Table 2. The majority of the calculated $\sigma_{S,N}$ are smaller than 0.1, which implies that in most cases the curvature corrections give reliable results for the range of frequencies $0.3\nu_l < \nu < 1.3\nu_h$, considering a typical synchrotron spectrum with $\alpha = -0.5$. We use the measured $\sigma_{S,N}$ and the corresponding ranges of $\xi(\alpha, \kappa)$ for calculating the final estimates of the spectral parameters and deciding whether these estimates should be treated as the values of, or only the limits on the respective quantities.

EDITOR: PLACE TABLE 2 HERE.

3. Properties of the synchrotron spectra of the jet components

Table 2 lists the derived values and limits (shown in brackets) of the synchrotron spectra in the VLBI core and jet components C2, C3, C4, and C5. For each feature and epoch, the table also shows the spectral index, α_{fit} of the fitted synchrotron spectra, and gives the limits on the bulk Lorentz factors and luminosities of the features, which will be discussed in section 3.2. Figure 4 illustrates the fitting results for the component C5. The dotted lines represent third order polynomial fits to the data. The solid lines show the synchrotron spectra derived after the application of the local curvature corrections described in section 2.3.1. If the spectral turnover is covered by the data (epochs 1987.3, 1988.2 in Figure 4), the curvature corrections were applied at the turnover point obtained from the polynomial fit. In other cases, the corrections were applied at the lowest observed frequency. For the datasets containing only two spectral points, only crude estimates of upper limits of ν_m and lower limits of S_m were made (these estimates are largely determined by the typical ν_L and ν_H inferred from the fits to other datasets for C5). We will base our discussion of the spectral evolution on the derived spectral properties of the core and C5 for which the spectral data are most complete (we will also make some remarks on C4 for which we have only 4 epochs with estimated values of ν_m and S_m . For C2, C3, and C4, largely represented by the limiting values, only the luminosity estimates will be discussed.

EDITOR: PLACE FIGURE 4 HERE.

3.1. Evolution of the turnover frequency

Figures 5–6 present the fitted turnover frequencies and flux densities for C4, C5, and D. C4 is represented mostly by the limiting values of S_m and ν_m . The data for C5 are

more complete. In the core, the highest values of ν_m (> 20 GHz) may be underestimated, owing to the uncertainty in determining the spectral index in cases when only the optically thick part of spectrum is sampled. The discrepancy between the derived values and lower limits of S_m in C4 indicates that the fits to the two-point spectral datasets may suffer from systematic errors.

The increases of the turnover frequency of the core do not precede or accompany the ejection of new jet components, but rather occur some time after the ejections. At the epochs when the components were first detected (1980.2: C4, 1983.1: C5—BMC86; 1989.2: C6,C7—Bååth et al. 1992), the turnover frequency in the core was comparatively low. The changes of S_m in the core are correlated with the flux density variations in the core and with the changes in total flux density at 22 GHz (although the correlation with the total flux density is weaker, owing to substantial contributions of the jet components; L96).

The situation is different in C5. Between 1984 and 1990, the turnover flux density of C5 remained within the range of 3.8–5.6 Jy, whereas the 5, 8, and 22 GHz flux densities of the component were varying between 1 and 6 Jy (L96). This suggests that the observed spectrum could be significantly affected by Doppler boosting. The turnover frequency of C5 shows a peak in time, with the maximum occurring between 1985.8 and 1988.2. The variations of ν_m may be similar in C4, if we consider the upper limits in 1981.8 and 1982.4.

EDITOR: PLACE FIGURE 5 HERE.

EDITOR: PLACE FIGURE 6 HERE.

3.2. Luminosity and kinematics

The luminosities of the core, and the jet components C2–C5 can be derived from the measured S_{int} which does not require the turnover frequency to be known. The kinematic parameters of the jet components can be inferred from the polynomial fits to their observed component trajectories (L96). Since S_{int} is an integral quantity, the anisotropy of relativistically beamed emission cannot be accounted for by the commonly used $\delta^{2-\alpha}$ correction, because the turnover point is often located within the 4–25 GHz frequency limits, and the spectral index changes within the range of integration. To account for the anisotropy of the emission, we calculate the fraction, $\Omega/4\pi$, determined by the solid angle, Ω , which contains most of the beamed emission. We use the measured apparent velocity, β_{app} and determine the minimum Lorentz factor $\gamma_{\text{min}} = (1 + \beta_{\text{app}}^2)^{1/2}$ that can reproduce the observed β_{app} . Under this condition, the component kinematics are defined solely by γ_{min} ,

since $\sin \theta = 1/\gamma_{\min}$ and $\delta = \gamma_{\min}$, where θ is the angle between the velocity vector of the component and the line of sight. This gives an upper limit for the 4–25 GHz luminosity

$$L_{4-25\text{GHz}} \approx \frac{8\pi c^2 S_{\text{int}}}{H_0^2} \left[1 - \cos \left(\frac{1}{\gamma_{\min}} \right) \right] \left[1 + z - \sqrt{1 + z} \right]^2 . \quad (5)$$

EDITOR: PLACE FIGURE 7 HERE.

The derived luminosities and minimum Lorentz factors are given in Table 2. Figure 7 shows the luminosity changes in the core and the jet components. We estimate $\gamma_D \approx 3.5$, assuming that the Lorentz factor of the core is similar to the initial Lorentz factors of the moving components (ZCU95). This yields $L_D = (7.1 \pm 3.5) \cdot 10^{42} h^{-2} \text{ erg s}^{-1}$ for the average luminosity of the core. We estimate the total 4–25 GHz luminosity of the jet features as $L_{\text{jet}} \approx 3 \cdot 10^{43} h^{-2} \text{ erg s}^{-1}$, which amounts to about 1% of the observed luminosity of 3C345 in the radio to infrared range (Bregman et al. 1986). The average decrease rate for all components is $\approx 1.2 \cdot 10^{35} h^{-2} (0.74 \pm 0.06)^{t-1979.0} \text{ erg s}^{-2}$ (we use the 1981–88 data to determine the luminosity decrease in the core). The derived rates of decrease are given in Table 3. Comparable rates of energy losses in different jet components imply similar physical conditions. The only exception to the observed similarity is the luminosity of C4 which decreases almost twice as fast. This difference can be caused by several factors:

EDITOR: PLACE TABLE 3 HERE.

1) Because of the narrow observed frequency range, the derived luminosities might not adequately reflect the physical conditions in the jet, and the observed regularities might be coincidental. However, most of the component spectra have their maxima within or near the 4–25 GHz range, so that their evolutions must be similar in order to produce comparable rates of decrease of the luminosity.

2) It is possible that we are underestimating the Lorentz factors of the components C2, C3, and C5. However, it would require very high Lorentz factors ($\gamma_{C3} \approx 35$, $\gamma_{C5} \approx 26$), to match the slope of C4. Here, we have taken the luminosities of C3 and C5 at their first epochs, and calculated their expected luminosities at 1993.0, assuming that the components had the same rate of decrease as that of C4. From the calculated luminosities, the required Lorentz factors were determined, using equation 5. The derived γ_{C3} and γ_{C5} are considerably higher than the theoretical limits on the bulk Lorentz factor expected in a jet ($\gamma \approx 20$; Abramovicz 1992; Henri and Pelletier 1992).

3) C4 might represent a composition of two possibly related features in the jet. The observations made in 1984–86 indicate that C4 could be a blend of two emitting regions

(ZCU95). The compound nature of C4 is not obvious at later epochs, and we can suggest that a weaker subcomponent could not be distinguished from the emission of a stronger and faster main subcomponent (C6 and C7 may represent a similar situation: the faster and younger C7 overtakes the older and slower C6; Lobanov 1996). This might result in an increase of the measured proper motion and, correspondingly, in higher values of γ_{\min} .

EDITOR: PLACE FIGURE 8 HERE.

The implications of the faster decrease in luminosity observed in C4 can be understood better, if we study the evolution in the luminosity along the jet. Figure 8a presents the correlations between the derived luminosities of the components and the apparent distance traveled along the jet

$$R_{\text{app}}(t) = \int_0^t \mu(t) dt, \quad (6)$$

where $\mu(t)$ is the proper motion of the component, and $t = 0$ refers to its epoch of ejection. Figure 8a shows that the luminosities of C2, C3, and C5 depend on R_{app} in a similar fashion, so that it is possible to find a general trend for the decrease of luminosity in the jet on the scales of up to 8 mas. The linear fit to this trend, represented by the solid line in Figure 8a, corresponds to $\log(L_{C2,3,5}) = 42.91 - 0.29 R_{\text{app}}$. The same procedure applied to C4 yields $\log(L_{C4}) = 44.35 - 0.66 R_{\text{app}}$. All fits are described in Table 4.

EDITOR: PLACE TABLE 4 HERE.

We now investigate whether the luminosities of the jet components are better correlated in the rest frame of the jet. In order to study the luminosity evolution in the rest frame of the jet, certain assumptions must be made about the component kinematics. We consider the luminosity evolution in a curved jet with constant and variable component speeds. In the rest frame of the jet, the jet component travels the distance

$$R_j(t) = (1 + z)^{-1} \int_0^t \frac{\beta(t)}{1 - \beta(t) \cos \theta(t)} dt. \quad (7)$$

The time variations of the component speed β and viewing angle θ are determined by the measured β_{app} and the chosen evolution of the Lorentz factor.

The observed trajectories of the components cannot accommodate a single value of Lorentz factor γ_{jet} , for all jet components, unless $\gamma_{\text{jet}} \geq 20$ (L96). We find that adopting $\gamma_{\text{jet}} = 20$ does not improve the agreement between C4 and other jet features. If the individual Lorentz factors of the jet components are allowed to be different, the kinematic constraints from the observed component trajectories require that $\gamma_{C5} \geq 7$, $\gamma_{C4} \geq 15$, $\gamma_{C3,C2} \geq 20$ (L96). We adopt these constraints and plot the resulting rest frame luminosity

evolution in Figure 8b. The component luminosities in Figure 8b are not well correlated (see Table 4 which lists the corresponding rates of decrease of the luminosities). At comparable distances, the luminosities of different components can differ by more than one order of magnitude. The decrease in the luminosity of C5 is also faster than in other components. These discrepancies suggest that the Lorentz factors of the components may vary along the jet. To illustrate that, we consider a jet that carries the least kinetic power, so that each component in the jet always moves at its respective γ_{\min} , as determined from the variations of the observed β_{app} . The resulting $\gamma(R_j)$ tracks are shown in Figure 8d. The corresponding luminosities of the components are presented in Figure 8c. The solid line in Figure 8c represents overall decrease in luminosity $\log(L_{\text{jet}}) \approx 42.06 - 0.03 R_j$ derived for all the components. With exception of C2 (for which the calculations of luminosity may be not reliable), the individual evolutions of the components do not deviate significantly from the overall decrease (see Table 4). Assuming that the mechanism of emission is the same in all of the components in the jet, the observed similarity of the decrease in luminosities of the components suggests that the Lorentz factor should change along the jet, in order to explain the variations of these luminosities. The intrinsic accelerations are also required from the kinematic constraints in the jet (Lobanov & Zensus 1996). Unwin et al. (1997) find that the component C7 in the jet must accelerate from $\gamma \approx 5$ to $\gamma \approx 10$ in order to reproduce the X-ray variations observed in 3C 345. The derived rate of acceleration of C7 is then consistent with the changes in γ_{\min} in C3 and C4.

4. Spectral evolution in the relativistic shock model

Consider a relativistic shock propagating down a conical jet with a constant half-opening angle ϕ . The shock expands sideways adiabatically, and maintains the condition of a plane shock, so that its longitudinal dimension is much smaller than the transversal. A power-law distribution of the energy of electrons, $N(\gamma)d\gamma \propto \gamma^{-s}d\gamma$, is assumed. With increasing distance, R , from the origin of the jet, the magnetic field decreases as R^{-a} , with $a = 1$ for the field perpendicular to the jet axis, and $a = 2$ for the field parallel to the axis (intermediate values of a are also possible). The shock passes through three basic evolutionary stages at which its emission is subsequently dominated by the Compton, synchrotron and adiabatic losses (Marscher, Gear, & Travis 1991). In the observer's frame, the received spectrum of the shock emission can be written in the form:

$$S(\nu) \propto R^\xi \nu^{-\zeta} \delta^{(s+3)/2}, \quad (8)$$

where ξ and ζ describe different stages of evolution of the shock. The turnover flux density is:

$$S_m \propto B^{-1/2} \nu_m^{5/2} R^2 \propto R^{(4+a)/2} \nu_m^{5/2} \quad (9)$$

(Cawthorne 1991). We further assume that the Doppler factor $\delta \propto R^b$, where b is constant. Combining (8) and (9), we obtain for the turnover frequency

$$\nu_m \propto R^{[\xi-(4+a)/2+b(s+3)/2]/[5/2+\zeta]} . \quad (10)$$

Using ξ and ζ calculated by Marscher (1990), we write expressions for ν_m and S_m at each stage of the evolution of the shock.

1) Compton–loss stage ($\xi = [(11 - s) - a(s + 1)]/8$; $\zeta = s/2$)

$$\nu_m \propto R^{-[(5+s)(a+1)-4b(s+3)]/[4(s+5)]} , \quad (11)$$

$$S_m \propto \nu_m^{[(a-11)(s+5)-20b(s+3)]/[2(s+5)(a+1)-8b(s+3)]} . \quad (12)$$

2) Synchrotron–loss stage ($\xi = -[4(s - 1) + 3a(s + 1)]/6$; $\zeta = s/2$)

$$\nu_m \propto R^{-[3a(s-1)+4(s+2)-3b(s+3)]/[3(s+5)]} , \quad (13)$$

$$S_m \propto \nu_m^{[3b(3s+10)-(3a+2)(2s-5)]/[3b(s+3)-3a(s-1)-4(s+2)]} . \quad (14)$$

3) Adiabatic–loss stage ($\xi = [2(5 - 2s) - 3a(s + 1)]/6$; $\zeta = (s - 1)/2$)

$$\nu_m \propto R^{-[2(2s+1)+3(a-b)(s+2)]/[3(s+4)]} , \quad (15)$$

$$S_m = \nu_m^{[(19-4s)-3a(2s+3)+3b(3s+7)]/[3(b-a)(s+2)-2(2s+1)]} . \quad (16)$$

R in formulae 11–16 is still measured in the rest frame of the jet, and should be transformed to the observer’s frame, using equation (7).

We now consider the observed changes of S_m and ν_m in the jet of 3C 345 in the framework of the dependencies (11)–(16). For simplicity, we assume $a \approx const$, and $s \approx const$. Spectral changes in a shock can be then described by three parameters: ρ ($S_m \propto \nu_m^\rho$), ε ($\nu_m \propto R^\varepsilon$), and b ($\delta \propto R^b$) which we will also be calling the b –parameter. Figure 9 illustrates the relations between ρ , ε , and b , for each evolutionary stage of the model. The shown curves do not differ significantly, for conceivable ranges of a ($1 < a < 2$) and s ($1 < s < 3$).

EDITOR: PLACE FIGURE 9 HERE.

4.1. The VLBI core

The spectral evolution of the core is shown in Figure 10. We are unable to find suitable model parameters for two intervals: 1982.4–1984.2 and 1989.2–1990.2. Incidentally, these intervals cover the ejections and first detections of C5 and C6,7. In these time intervals,

the ν_m of the core is rising, while the S_m is nearly constant, or even decreasing slightly. According to the adopted model, it is impossible to have $\varepsilon > 0$ and $\rho < 0$ simultaneously (see Figure 9). This implies that ν_m cannot increase while S_m decreases (also ruling out fitting the overall downward trend seen in the period 1982–90 in the core spectrum). Figure 9 shows that S_m and ν_m can increase simultaneously only if $\rho \geq 2.5$. In the two time intervals mentioned above, $\rho \sim 0$, so ν_m must decrease. It is possible that the time sampling of the spectral data is too poor to adequately represent the changes in the core. Alternatively, the core may also represent a characteristic region in relativistic flow. For instance, it can be the location at which $\tau = 1$ and the jet becomes optically thin. In this case, during the time between two successive ejections of new jet features, the spectral changes in the core are not necessarily consistent with those of a shock.

EDITOR: PLACE FIGURE 10 HERE.

EDITOR: PLACE TABLE 5 HERE.

The shock model is more successful in reproducing the decay stages (1981–82, 1984–89) and the rise and fall in 1990–1993. Table 5 gives the values of ρ , b and ε corresponding to the tracks A, B and C in Figure 10. In the core, the jet axial coordinate R has only a limited meaning, since the core is believed to be stationary. One can possibly relate R to the time measured in the observer’s frame, but the actual proportionality is not obvious. In view of that, the derived $\delta(R)$ and $\nu_m(R)$ dependencies can reflect the magnitude of Doppler factor and turnover frequency variations only indirectly. It is, however, symptomatic that the largest variations of δ and ν_m are required during the Compton–loss and adiabatic–loss stages, whereas more moderate changes describe the synchrotron–loss stages.

Assuming that the core is associated with the $\tau = 1$ region of the jet, the calculated ρ , b and ε may be reconciled with the following scheme:

1990.2–91.8: a dense relativistic plasma condensation produced by an outburst in the nucleus gradually becomes visible, as it enters the $\tau = 1$ region. If a shock is formed at this stage, the increased plasma density, strong Compton losses and shock acceleration should lead to increases in both S_m and ν_m . This is reflected in $\rho > 0$, $b > 0$, $\varepsilon > 0$. If the initial density of the plasma condensation is not large enough, the formation of a shock may be delayed and ν_m may rise without significant changes in S_m (1982.4–84.2; 1989.3–90.2).

1991.8–92.5; 1984.2–85.8: the entire condensation is inside the core region. The plasma density remains constant (or decreases slightly), and $b \sim 0$. Synchrotron losses dominate the emission, so that ν_m falls off ($\varepsilon < 0$), and S_m changes weakly ($\rho \sim 0$). The most advanced parts of the condensation begin to be seen as a separate feature receding from the core.

1992.5–93.8; 1985.8–89.2: the condensation leaves the core region; the plasma density decreases rapidly. This can mimic an adiabatic expansion, and cause both ν_m , and S_m to fall off substantially. The steepest possible model slope $\rho = 2.9$ (if $b \rightarrow -\infty$) still falls short of representing the nearly vertical downfall of S_m ($\rho \sim 10$) in 1985.8–89.2. If the emission is still dominated by the synchrotron losses, it would require the plasma number density, $N_0 \approx R^{-4}[N_0]_{\text{adiabatic}}$ to reproduce the data. It appears, therefore, that the adiabatic expansion should be complemented by the recession of the plasma condensation from the core.

4.2. The components C4 and C5

In the jet components, the changes of the b -parameter required by the shock model can be compared with the values derived from the component trajectories. The S_m - ν_m tracks can also be tested against the observed component trajectories and apparent speeds.

4.2.1. S_m - ν_m evolution in C4 and C5

The S_m - ν_m tracks of C4 and C5 are shown in Figure 11. The corresponding model parameters are listed in Table 5. The data for C4 are too sparse. The slope $S_m \propto \nu_m^{2.8}$ in 1983.4–88.2 gives uncomfortably low values of $\varepsilon = -7.8$ and $b = -9.7$. The derived b is inconsistent with the component kinematics (Figure 13). The last section of the component spectral track can be approximated by a moderately accelerating shock in the adiabatic-loss stage.

The data for C5 are more complete, and the component's S_m - ν_m track can be divided into three sections corresponding to the main stages of shock development. Only the 1984.2–85.8 fraction of the track is problematic for fitting: ν_m is rising, while S_m is decreasing. In connection with the spectral changes seen in the core in 1982–85, we can speculate that a strong shock did not begin to form until about 1985. At later times, we can describe the spectral changes in C5 as follows (see Table 5 for the corresponding model parameters):

EDITOR: PLACE FIGURE 11 HERE.

1985.8–88.2: Compton-loss stage, with moderate acceleration ($b = 2.0$). The component rest frame distance increases during this period by $R_{88.2}/R_{85.8} \approx 1.1$. The kinematic value of the b -parameter is ≈ 1 (adopting the $\gamma = \gamma_{\text{min}}(t)$ evolution of the component Lorentz factor; see Figure 13). If we take $b = 1$, then $S_m \propto \nu_m^{14.2}$ which is too steep to match the data.

1988.2–89.2: synchrotron–loss stage, with constant Doppler factor ($b = 0$). Adoption of the kinematic $b(\gamma_{\min}) \approx 1$ would result in $S_m \propto \nu_m^{-8.2}$ which is unrealistic. In one year, ν_m changes from ≈ 7 GHz to ≈ 3 GHz, which corresponds to $R_{89.2}/R_{88.2} \approx 2.3$.

1989.2–92.5: adiabatic–loss stage, with $b = -2.6$ ($R_{92.5}/R_{89.2} \approx 1.6$). The S_m – ν_m slope in the data appears to be steeper than the model value $\rho = 1.8$, but the increased errors allow for $\rho = 0.9 - 2.6$. In Figure 13, the $b(\gamma_{\min})$ of C5 decreases in 1989.2–92.5, but it matches the model value only in 1992. If γ_{C5} is constant, the corresponding b –parameter increases (as shown in Figure 13 for $\gamma_{C5} = 7$; similar curves result from other constant values of γ_{C5}).

4.2.2. Kinematic b –parameters of the jet components

We derive the component trajectory and kinematic parameters using the measured component position offsets ($x(t), y(t)$) from the core (see ZCU95 for more details). Figure 12 shows the observed offsets and the derived trajectory of C5. From the trajectory, the component proper motion, $\mu(t) = [(dx/dt)^2 + (dy/dt)^2]^{1/2}$ and apparent speed, $\beta_{\text{app}}(t) = \mu(t)D_L(1+z)^{-1}$ can be calculated. If the component Lorentz factor is known, the corresponding three–dimensional trajectory can be reconstructed. Several possible cases of the evolution of the Lorentz factor have been discussed in section 3.2. In addition to those, we now also consider the Doppler factors variations that can be deduced from the observed spectral variations. For given $\gamma(t)$ or $\delta(t)$, we can determine the corresponding b –parameter variations, and compare them with the model predictions. The kinematic b –parameters must be measured locally, because of the substantial and non–monotonic variations of the measured apparent speeds. We use

$$b(t) = \frac{\log[\delta(t+dt)/\delta(t)]}{\log[R_j(t+dt)/R_j(t)]}, \quad (17)$$

where R_j is the rest frame traveled distance calculated from equation 7.

EDITOR: PLACE FIGURE 12 HERE.

4.2.3. Peaked evolution of the turnover frequency

We now compare the b –parameters derived from the observed tracks of C4 and C5 with their counterparts obtained from modeling the spectral changes in these components. The results of this comparison are presented in Figure 13. The dot–dashed lines in Figure 13 show the ranges of b –parameters for which a peak in the time evolution of ν_m is possible. In

both C4 and C5, the b -parameters corresponding to $\gamma_{\min}(t)$ lie within the derived ranges. Therefore, for both C4 and C5, the evolution of ν_m which shows a peak, can in principle be reconciled with the observed kinematic properties. However, the choice of $\gamma_{\min}(t)$ is arbitrary, and is not tied to the modeled spectral evolution.

Altogether, different phases of shock development can approximate the spectral changes seen in C5. However, as seen in Figure 13, the model b -parameters required by the adopted shock evolution do not match well the kinematic values derived for both the $\gamma = \text{const}$ and $\gamma = \gamma_{\min}$ cases. In the next section, we will discuss a self-consistent scenario for C5, based on both spectral and kinematic properties of the component.

EDITOR: PLACE FIGURE 13 HERE.

4.2.4. Spectral and kinematic evolution of C5

We now investigate how well a single set of model parameters can describe the observed spectral and kinematic changes in C5. If the turnover frequency changes between two epochs (t_1, t_2) from ν_1 to ν_2 , then

$$R_1 = \Delta R_j (\nu_1/\nu_2)^{1/\varepsilon} [1 - (\nu_1/\nu_2)^{1/\varepsilon}] \quad (18)$$

determines the location at which the component must be at t_1 in order to satisfy the observed $S_m(\nu_m)$ and the $\nu_m(R_j)$ required by the model. We consider two cases in which the initial Doppler factors are: $\delta_{01} = 1.05$ and $\delta_{02} = 2.8$. For these cases, we determine the R_1 at each stage of the spectral evolution in C5 (Table 6). The derived R_1 are much smaller for the synchrotron-loss stage (1988.2-89.2), compared to the values for the other two stages. This indicates that the spectral changes occurring in C5 during this period are too rapid to satisfy both the shock model and the observed kinematics. No satisfactory fit can be achieved by varying the model $S_m(\nu_m)$ slopes and durations of each of the stages of the evolution of the shock. Assuming that spectral points with $5 < \nu_m < 15$ GHz are the most accurate, we reproduce a self-consistent S_m - ν_m track (the dot-dashed line in Figure 11) which satisfies the observed trajectory of C5. It is clear, from Figure 11, that the modeled track cannot accommodate the rapid spectral changes in 1988-92. Variations in the initial Doppler factor δ_0 do not change the model track significantly. The shape of the track is chiefly determined by the rise in 1985-88. In that period, the only plausible deviation from the modeled shape is to make the rising slope shallower, and to attempt extending the flat section of the track (corresponding to the synchrotron-loss stage) by varying the b -parameter. The rising slope in 1985-88 can be made shallower only by forcing $\rho < 5.1$. As a result, the corresponding values of b grow significantly larger, and the length of the rising section of the track grows dramatically. This precludes finding any satisfactory

fit for the synchrotron and adiabatic stages of the shock, leaving no room for a successful shock-based scenario capable of explaining both the spectral and the kinematic properties of C5.

The difficulties in explaining the observed spectral and kinematic properties of C5 may be caused by several different factors. One possible explanation is that C4 and C5 could have been produced by the same outburst in 3C 345. The estimated ejection epochs of C4 and C5 differ only by about 0.5 year, yet the emission and kinematic properties of the two components are significantly different (L96). C4 is much faster and brighter, compared to C5. It is therefore possible that C4 and C5 represent the forward and reverse shocks propagating in the jet.³ There is also observational evidence for a possible transition occurring in the jet of 3C 345 at about 1.2–1.5 mas distance from the core (Lobanov & Zensus 1996). At this distance, the component proper motions, polarization properties and flux density behavior change. For the jet, this may indicate a change in the dominating emission mechanism (for instance, if at this distance strong shocks have already dissipated, and the jet emission properties become determined largely by interactions between the jet and the ambient medium). C5 has passed the 1.5 mas point in 1988.1; incidentally, this marks the time when applying the shock model to the spectral evolution of C5 becomes difficult.

EDITOR: PLACE TABLE 6 HERE.

5. The VLBI core as an inhomogeneous relativistic jet

As follows from section 4.1, relativistic shocks have noticeable difficulties reproducing the observed spectral changes in the VLBI core of 3C 345 within a single, self-consistent scheme. Variations of the particle number density—a free parameter in the shock model—appear to be necessary to fit the observed values. With this requirement in mind, we now apply, to the VLBI core, a modification of the quasi-steady, inhomogeneous relativistic jet model proposed by Königl (1981) to describe the emission from ultra-compact jets. In its original formulation, the model is stationary (i.e., it does not make specific predictions about the time variability of the emission), and because of this, it has been previously applied for fitting the core spectrum in 3C 345 only at single epochs: 1982.0 (ZCU95) and 1992.7 (Unwin et al. 1997).

³The first anonymous referee of the manuscript suggested that C5 could also be traveling through the plasma that has been shocked by C4. This could weaken the emission of C5, and alter its spectral evolution.

In order to permit self-consistent fits to multi-epoch data, we need to make several assumptions about those model parameters which are unconstrained by the spectral data. We assume that a relativistic plasma with spectral index $\alpha_0 = -0.5$ is continuously injected into the jet with bulk Lorentz factor γ_j . The jet is unresolved (which also follows from the measured sizes of the core, as reported in ZCU95 and L96). The jet geometry is approximated by a cone with an opening angle $\phi_j \approx \text{const}$. The axis of the cone forms an angle $\theta_j \approx \text{const}$ with the line of sight. The jet plasma is characterized by a tangled magnetic field, $B = B_1 R^{-a}$, and particle density, $N = N_1 R^{-n}$ (here B_1 and N_1 are measured at $R = 1$ pc). The number of particles is conserved, and the particle energy density in the jet, u_p , is in approximate equipartition with the magnetic field energy density, u_B , so that $u_p = q_e u_B$ (with $q_e \sim 1$, but possibly varying from one epoch to another). This implies that $a = 1$, $n = 2$, and $N_1 = q_e B_1^2 (8\pi m_e c^2)^{-1}$ (where m_e is the electron mass, and c is the speed of light). Finally, we must take into account the effect of changes in the optical depth, from one epoch to another, expressed by the distance, $r_m \propto \delta^{-1/6} N_1^{1/6} B_1^{11/6}$, at which the jet becomes optically thin for the synchrotron radiation. With this additional requirement (and for the choice of parameters described above), the observed variations of the turnover point of the synchrotron spectrum of the VLBI core should comply with the following relations:

$$S_m = C_S N_1^{0.42} B_1^{4.08} \delta^{5.08}, \quad (19)$$

$$\nu_m = C_\nu N_1^{0.17} B_1^{-0.17} \delta^{0.83}. \quad (20)$$

To simplify further discussion, we will drop C_S and C_ν (both of them vary weakly with respect to γ_j , and are constant with respect to our choice of other model parameters). We then consider only fractional changes of N_1 , B_1 , and δ , by taking their respective values at the first spectral epoch ($t_0 = 1981.5$) as unity. One has to make an assumption about the changes of one of these three quantities, in order to reconstruct the evolution of the other two. We take $\delta = \text{const}$ as the most plausible assumption, relying again on the similarity between the measured apparent jet speeds in the immediate vicinity of the core (ZCU95, L96). This assumption makes it possible to determine the changes of N_1 required to reproduce the observed spectral variations. These changes are plotted with open circles in Figure 14. The relative peak-to-peak variations of N_1 do not exceed 500. The corresponding magnetic field varies within 20%, making the proposed scheme rather attractive. We therefore conclude that moderate variations of the particle density in an unresolved, inhomogeneous jet with constant Doppler factor can explain the observed spectral variations in the VLBI core of 3C 345.

EDITOR: PLACE FIGURE 14 HERE.

5.1. Flare model for the particle density variations

We will attempt now to find out whether the determined changes of N_1 can be accommodated within a simple and self-consistent description of density variations in the jet. To represent the changes of N_1 , we use flare-like events described by an exponential rise and decay of the density, so that $N(t) = N_{\text{rel}} \exp(t_\tau)$, where $t_\tau = |t - t_{\text{flare}}| \tau_{\text{flare}}^{-1}$. Here t_{flare} and τ_{flare} refer to the epoch and duration of the flare, and $N_{\text{rel}} = N_{\text{flare}}/N_{\text{quiescent}}$ is the relative density increase during a flare. We take $N_{\text{quiescent}} = 1$, and find that the changes of N_1 determined in the previous section can be represented by a sequence of 5 flares occurring roughly every 3.5–4 years. The parameters of the flares are listed in the “spectrum” section of Table 7. The density variations resulting from these flares are represented by the dotted line in Figure 14. Figure 14 also shows the variations of the Doppler factor (open squares) and magnetic field (filled triangles) that correspond to the sequence of the flares obtained. The epochs of the flares and their relative strengths are shown in Figure 14 by stars and segments. We are not able to find a satisfactory fit to the density at the last spectral epoch (1993.8), without introducing a flare in 1995. Since the flares in 1981 and 1995 are not constrained by the spectral data, we use dashed-line trapeziums to illustrate the allowed ranges of epochs and strengths of these flares. The rather large values of N_{rel} suggest that the quiescent particle density in the jet is likely to be small: the jet material should then be supplied entirely by the flares. In this case, one can expect a strong correlation between the occurrence of the flares and variability of the total radio emission. To illustrate this, we plot also the 22 GHz light curve in Figure 14 (in order to better place the light curve within the plot, we scale the fluxes down by a factor of 100). The total flux evolution agrees well with the flare model: the much weaker flare at 1987.8 has resulted in the dramatic decline of the total emission (around 1990, the radio emission from 3C 345 was at its all-time low). Conversely, the subsequent, stronger flares in 1992 and 1995 are noticeably reflected by the increased total flux density.

With regard to the scheme presented above, we would like to stress that the suggested sequence of the flares is not strictly a fit to the data. Sparsity of the spectral epochs does not warrant proper fitting. In addition, our flare model is based on the assumption of $\delta = \text{const}$ which may (in general) be relaxed, possibly altering the derived flare parameters. However, we find it rather remarkable and attractive that varying only a single parameter (N_1) of the model can be sufficient for explaining the entire observed spectral evolution in the VLBI core, and that the variations of N_1 can be represented by a rather regular sequence of flare-like events occurring in the nucleus of 3C 345.

EDITOR: PLACE TABLE 7 HERE.

5.2. Applying the flare model to the light curves

We now attempt to apply the flare model to reproduce the emission variations at 22 GHz. The total emission is not well suited for this purpose, because it contains, even at 22 GHz, significant (20–50%) contributions from the jet components. We therefore choose to fit the flare model to the flux density variations of the VLBI core. The available flux density data for the VLBI core cover the time period from 1981 until 1997, continuing for 3 years after the last spectral epoch (1993.8), and sampling well the flare in 1995.

To describe the flux density changes during a flare, we consider the synchrotron emission from a stationary adiabatic flow, confined by the pressure, $p \propto R^{-4\epsilon}$, of the external medium (Georganopoulos & Marscher 1996). The emission can then be described by equation 1, with $\nu_1(t)$ incorporating the adiabatic and synchrotron energy losses in the plasma:

$$\nu_1(t) = \nu_{1,0} \left[\left(1 + \frac{\beta_j \delta_j}{R_{\text{core}}} (t - t_{\text{flare}}) \right)^{(2\alpha-3)\epsilon} N_{\text{rel}} \exp(t_\tau) \right]^{2/(5-2\alpha)}. \quad (21)$$

We assume $\nu_{1,0} = 10$ GHz and $\epsilon = 1/3$. The kinematic conditions are described by $R_{\text{core}} \approx 3.5$ pc (Lobanov 1998a) and $\delta_j \approx 6$ (from $\gamma_j \approx 3.5$ and $\theta_j \approx 5^\circ$ typically measured in the vicinity of the VLBI core). We take the previously obtained flare sequence as a starting model, and adjust the flare parameters so as to fit the core flux densities. The resulting fit gives a remarkably good approximation of the observed flux density changes in the core. We plot the obtained fit in Figure 15, together with the variations of the total and VLBI core flux densities. The parameters of the flares are given in the “light curve” section of Table 7.

The discrepancies between the epochs and durations of the “spectral” and “light curve” flares are small, with exception of the weak flare in 1986–87 for which fitting is difficult in both cases. The “spectral” flare in 1992.5 is not constrained by the data, which can explain why its density increase differs from that found in its counterpart “light curve” flare. The densities inferred from the “light curve” flares give a better representation of the density changes in the jet, since these flares are derived from the measured values of the flux density (in contrast to the “spectral” flares which describe the modeled relative changes of the particle density). The density increase in the “light curve” flares is up to 10 times larger than in their “spectral” flare counterparts, further enhancing the argument that flares supply the major fraction of the material carried by the jet.

Noticing the remarkable overall regularity of the flare events in 3C 345, we can venture to predict that the next flare (already visible in the 22 GHz light curve in Figure 15) should peak at around mid–1999, with the total flux density reaching at least 16 Jy. It is conceivable that the flare sequence seen in 3C 345 results from physical settings similar to those uncovered in OJ 287 (Valtonen & Lehto 1997), where the observed quasi–periodical variations of radio emission are likely to be caused by the orbital motion in a binary black hole system. This argument, however, lies outside the scope of this paper, and will be

discussed elsewhere.

We limit ourselves here to remarking again on the simplicity and success of the obtained flare model which, for both spectral and flux density data, provides a satisfactory description relying only on variations of the particle density in the jet. The similarity of “spectral” and “flux density” flares also provides an additional argument for the fidelity of the spectral information obtained from the VLBI data.

EDITOR: PLACE FIGURE 15 HERE.

6. Summary

We have used the available multi-frequency VLBI observations to determine the basic properties of the synchrotron spectra of the enhanced emission regions in the parsec-scale jet of 3C345. The spectral information has been combined with the kinematic data, in order to derive suitable models for the observed evolution of the radio emission from the VLBI core and the moving components in the jet.

1. We have demonstrated that the compact jet emission can be adequately modeled by Gaussian components, used for fitting the interferometric visibility data obtained from VLBI observations. The models obtained can be combined into multi-frequency datasets, providing the necessary basis for studying the synchrotron spectra in the parsec-scale jet of 3C345.

2. The turnover frequency and the flux density can be recovered from multi-frequency datasets, using the measured curvature of the spectrum within the range of the observing frequencies, ν_l – ν_h . We have studied the limitations of the method and shown that it gives reliable results for turnover frequencies between $\sim 0.3\nu_l$ and $\sim 1.3\nu_h$, for data with flux density errors not exceeding 10%. Using this method, we have fitted the synchrotron spectra and estimated the turnover frequencies and the flux densities (or respective upper limits), for the VLBI core and the jet components in 3C345.

3. From the spectra obtained, we estimated the 4–25 GHz luminosities of the core and the jet components. The mean luminosity of the core is $\approx 7 \cdot 10^{42} h^{-2} \text{erg s}^{-1}$. The total luminosity of the parsec-scale jet in 3C345 is $\approx 3 \cdot 10^{43} h^{-2} \text{erg s}^{-1}$ which constitutes about 1% of the observed luminosity of the source in the radio to infrared regime. The observed luminosity changes indicate that the core and the jet components have comparable energy loss rates, and suggest that the jet components are accelerating in the rest frame of the jet.

4. The spectral evolution of the VLBI core differs from the changes seen in the spectra of the jet components. The spectral changes observed in the core can be partially

reproduced by a relativistic shock traveling through the region where the jet turns optically thin. A better description is provided by the framework of the inhomogeneous jet model which is capable of explaining the entire spectral evolution of the core by a sequence of flare-like events characterized by an exponential rise and decay of the particle density of the jet plasma. The same model is sufficient for explaining the observed flux density variations in the core of 3C 345. The model requires changes only one model parameter—the particle density in the jet—in order to reproduce the measured spectral and flux density data. The particle density variations obtained suggest that flares are likely to be supplying most of the material carried by the parsec-scale jet. The flares occur approximately once every 3.5–4 years, suggesting that a quasi-periodic process in the nucleus of 3C 345 may be driving the flaring activity. On the basis of the flare sequence determined, we can expect that the current flare, which began at the end of 1997, should peak in mid-1999, with the total flux density reaching at least 16 Jy.

5. There is a peak in the evolution of the turnover frequency of C5 (and possibly, C4). The peak in C5 can be reconciled with a moderately accelerating shock. The data are too poor to make any conclusion about C4. The kinematic properties of both C4 and C5 allow for the variations of the component Doppler factors required to produce a peak in the turnover frequency evolution. The shock-in-jet model has difficulties with reproducing the overall spectral and kinematic changes observed in C5. The spectral evolution is too rapid (especially at the later epochs) to be accommodated by the model, within the kinematic constraints determined by the component's observed trajectory. It is conceivable that the later epochs are marked by a rapid dissipation of the shock, although it remains difficult to single out the most likely cause for such an effect.

7. Acknowledgments

We would like to acknowledge P.E. Hardee, K.I. Kellermann, T.P. Krichbaum, A.P. Marscher and J. Roland for fruitful discussions during the course of this work. We thank I.I.K. Pauliny-Toth for many helpful comments on the manuscript. We also wish to thank the anonymous referees for numerous useful suggestions. We would like to acknowledge J.A. Biretta, M.H. Cohen, K.J. Leppänen, S.C. Unwin, and A.E. Wehrle for their valuable contributions to the long-term VLBI monitoring of 3C 345. JAZ acknowledges partial support by the Alexander von Humboldt Foundation's Forschungspreis. The National Radio Astronomy Observatory is a facility of the National Science Foundation operated under cooperative agreement by Associated Universities, Inc.

REFERENCES

- Abramovicz, M.A. 1992, in *Extragalactic Radio Sources: From Beams to Jets*, eds. J. Roland, H. Sol, & G. Pelletier (Cambridge: Cambridge University Press), 206
- Aller, H.D., Aller, M.F., & Hughes, P.A. 1996, in *ASP Conference Series, Vol.110, Blazar Continuum Variability*, eds. H.R. Miller, J.R. Webb, & J.C. Noble (San Francisco: ASP), 208
- Apostol, T.M. 1969, *Calculus*, v.1 (New York: John Wiley & Sons), p. 537
- Bååth, L.B., et al. 1992, *A&A*, 257, 31
- Babadzhanyants, M.K., & Belokon', E.T. 1984, *Astrophysics*, 20-21, 461
- Biretta, J.A., Moore, R.L., & Cohen, M.H. 1986, *ApJ*, 308, 93
- Blandford, R.D., & Rees, M.J. 1978, in *Pittsburgh Conference on BL Lac Objects*, ed. A.M. Wolfe (Pittsburgh: University of Pittsburgh), 328
- Bregman, J.N., et al. 1986, *ApJ*, 301, 708
- Cawthorne, T.V. 1991, in *Beams and Jets in Astrophysics*, ed. P.A. Hughes (Cambridge: Cambridge University Press), 187
- Cohen, M.H. 1985, in *Extragalactic Energetic Sources*, ed. V.K. Kapahi (Bangalore: Indian Academy of Sciences), 1
- Fichtel, C.E., et al. 1994, *ApJ*, 94, 551
- Georganopoulos, M., & Marscher, A.P. 1996, in *ASP Conference Series, v.100, Energy Transport in Radio Galaxies and Quasars*, eds. P.E. Hardee, J.A. Zensus, & A.H. Bridle, (San Francisco: ASP), 54.
- Halpern, J.P. 1982, Ph.D. thesis (Harvard University).
- Henri, G., & Pelletier, G. 1992, in *Extragalactic Radio Sources: From Beams to Jets*, eds. J. Roland, H. Sol, & G. Pelletier (Cambridge: Cambridge University Press), 221
- Hewitt, A., & Burbidge, G. 1993, *ApJS*, 87, 451
- Impey, C.D., & Neugebauer, G. 1988, *AJ*, 95, 307
- Kidger, M.R. 1990, *A&A*, 226, 9
- Kollgaard, R.I., Wardle, J.F.C., & Roberts, D.H. 1989, *ApJ*, 97, 1550
- Königl, A. 1981, *ApJ*, 243, 700

- Krichbaum, T.P., Witzel, A., Graham, D., et al. 1993 *A&A*, 275, 375
- Krichbaum, T.P., Alef, W., Witzel, A., et al. 1998 *A&A*, 329, 873
- Leppänen, K.J. 1995, Ph.D. Thesis, Helsinki University of Technology
- Lobanov, A.P. 1996, Ph.D. Thesis (NMIMT: Socorro, USA)
- Lobanov, A.P. 1998a, *A&A*, 330, 79
- Lobanov, A.P. 1998b, *A&AS*, 133, 261
- Lobanov, A.P., Carrara, E., & Zensus, J.A. 1997, *Vistas in Astronomy*, 41, 253
- Lobanov, A.P., & Zensus, J.A. 1994, in *2nd EVN/JIVE Symposium, Proceedings*, eds. A.J.Kus, R.T.Schilizzi, K.M.Borkowski, & L.I.Gurvits (Torun: University of Torun), 93
- Lobanov, A.P., & Zensus, J.A. 1996, in *ASP Conference Series, v.100, Energy Transport in Radio Galaxies and Quasars*, eds. P.E. Hardee, J.A. Zensus, & A.H. Bridle, (San Francisco: ASP), 124.
- Makino, F. 1989, in *AGN and the X-Ray Background. Proceedings of 23rd ESLAB Symposium*, eds. J.Hunt, & B.Batrich (Noordwijk: ESA), 803
- Malina, R.F., et al. 1994, *AJ*, 107, 2, 751
- Marscher, A.P. 1990, in *Parsec-scale Radio Jets*, eds. J.A. Zensus, & T.J. Pearson (Cambridge: Cambridge University Press), 236
- Marscher, A.P., Gear, W.K., & Travis, J.P. 1991, in *Variability of Blazars*, eds. E.Valtaoja, & M.Valtonen (Cambridge: Cambridge University Press), 85
- Moore, R.L., & Stockman, H.S. 1984, *ApJ*, 279, 465
- Pacholczyk, A.G. 1970, *Radio Astrophysics* (San Francisco: W.H.Freeman and Co.)
- Pearson, T.J. 1991, *BAAS*, 23, 991
- Pearson, T.J. 1996, in *ASP Conference Series, v.82: Very Long Baseline Interferometry and the VLBA*, eds. J.A. Zensus, P.J. Diamond, & P.J. Napier (San Francisco, ASP), 267
- Rabaça, C.R., & Zensus, J.A. 1994, in *Compact Extragalactic Radio Sources*, eds. J.A. Zensus, & K.I. Kellermann (Green Bank: NRAO), 163
- Ros, E., Zensus, J.A., Lobanov, A.P. 1999, *A&A* (in prep.)
- Steffen, W., Zensus, J.A., Krichbaum, T.P., Witzel, A., & Qian, S.J. 1995, *A&A*, 302, 335

- Tang, G., Bartel, N., Ratner, M.I., Shapiro, I.I., Bååth, L., & Rönnäng, B. 1990, in *Parsec-Scale Radio Jets*, eds. J.A.Zensus, & T.J.Pearson (Cambridge: Cambridge University Press), 32
- Teräsranta, H., Tornikoski, M., Mujunen, A., et al. 1998, *A&AS*, 132, 305
- Unwin, S.C., Cohen, M.H., Pearson, T.J., Seielstad, G.A., Simon, R.S., Linfield, R.P., & Walker, R.C. 1983, *ApJ*, 271, 536
- Unwin, S.C., & Wehrle, A.E. 1992, *ApJ*, 398, 74
- Unwin, S.C., Wehrle, A.E., Urry, C.M., Gilmore, D.M., Zensus, J.A., & Rabaça, C.R. 1994, *ApJ*, 432, 103
- Unwin, S.C., Wehrle, A.E., Lobanov, A.P., Zensus, J.A., Madejski, J.M., Aller, M.F., & Aller, H.D. 1997, *ApJ*, 480, 596
- Valtonen, M., & Lehto, H. 1997, *ApJ*, 481, 5
- Vio, R., Cristiani, S., Lessi, O., & Salvadori, L. 1991, *ApJ*, 380, 351
- Waltman, E.B., Fiedler, R.L., Johnston, K.J., Spencer, J.H., Florkowski, D.R., Josties, F.J., McCarthy, D.D., & Matsakis, D.N. 1991, *ApJS*, 77, 379
- Wardle, J.F.C., Cawthorne, T.V., Roberts, D.H., & Brown, L.F. 1994, *ApJ*, 437, 122
- Worrall, D.M., & Wilkes B.J. 1990, *ApJ*, 360, 396
- Zensus, J.A., Cohen, M.H., & Unwin, S.C. 1995, *ApJ*, 443, 35
- Zensus, J.A., Krichbaum, T.P., & Lobanov, A.P. 1995, *Publications of the National Academy of Sciences*, Vol. 92, Number 5, *Quasars and Active Galactic Nuclei: High Resolution Imaging*, eds. M.H. Cohen, & K.I. Kellermann, p. 11347
- Zensus, J.A. 1997, *ARA&A*, 35, 607

Fig. 1.— The top image: VLBI image of 3C345 at 3.6cm (Lobanov 1996). The contour levels are $-0.1, 0.1, 0.2, 0.3, 0.5, 1, 2, 3, 5, 10, 25, 50, 75,$ and 90% of the peak, 4.952 Jy . The bottom image: Gaussian model fit representation of the VLBI image, obtained by fitting 8 elliptical Gaussian components to the visibility data and optimizing the fit to the amplitudes and closure phases. Labeled are the VLBI stationary core D, and the components C7, C6, C5, C4, C3 and C2 embedded in the jet. The weakest and most extended jet feature, C1, lies outside the plotting range, at a distance of $\sim 20\text{ mas}$.

Fig. 2.— Example of fits to VLBI visibility data. The visibility amplitudes on two baselines (top) and closure phases on two triangles (bottom) are taken from the VLBI dataset used for producing the images in Figure 1. In the left panels, CLEAN component model is fitted to the visibilities; the right panels show the fit obtained by modeling the source structure with 8 elliptical Gaussian components. Consistency of the fits by the CLEAN and Gaussian model warrants the use of Gaussian model fits for describing the mas-scale structures in 3C345.

Fig. 3.— Theoretical curvature, κ , of the functional form (1) describing the homogeneous synchrotron spectrum with spectral index α . The ξ axis is the ratio of the frequency at which the curvature is calculated to the turnover frequency. Different symbols mark the smallest measurable curvature, κ_{\min} , for a spectral dataset with the given fractional flux density error. The meaningful corrections can be achieved for values of $\kappa \leq \kappa_{\min}$.

Fig. 4.— Spectral fits to the C5 data. Dotted lines are third order polynomial fits used for measuring the local curvature. Solid lines are the derived synchrotron spectra. The curvature is measured at the lowest observed frequency, unless the turnover is seen in the data (epochs 1987.3, 1988.2). In the latter case, the curvature is measured at the turnover frequency derived from the corresponding polynomial fit. When only two spectral points are available (epochs 1991.7, 1993.8), the fitted values represent the upper limits on the turnover frequency.

Fig. 5.— Evolution of the turnover frequency ν_m in the core and the jet components C4 and C5. For each feature, arrows mark the upper limits.

Fig. 6.— Evolution of the turnover flux density S_m in the core and the jet components C4 and C5. For each feature, arrows mark the lower limits.

Fig. 7.— Evolution of the luminosity in the VLBI core and the jet components. The shown luminosities are the upper limits derived from the measured integrated fluxes in the range of $4\text{--}25\text{ GHz}$, S_{int} , and estimated minimum Lorentz factors, γ_{\min} , listed in Table 2.

Fig. 8.— Luminosities and kinematics of the jet components: **a)** luminosities and apparent traveled distances; the dot-dashed line is a linear fit to C4 data; the solid line represents a linear fit for C2, C3, and C5 data combined. **b)** luminosities and rest frame traveled distances; the components move at constant speeds, $\gamma_{C2,3} = 20$, $\gamma_{C5} = 7$, $\gamma_{C4} = 15$. **c)** the

same as b), but each component moves at its $\gamma_{\min}(t)$. **d)** variations of $\gamma_{\min}(t)$ in the jet components in the rest frame of the jet.

Fig. 9.— Parameter space of the shock-in-jet model. The power indices ρ ($S_m \propto \nu_m^\rho$) and ε ($\nu_m \propto R^\varepsilon$) are shown for different values of b ($\delta \propto R^b$), for the three basic stages of the evolution of the shock. The dependencies shown are calculated for $a = 1$ and $s = 2.4$; the respective dependencies for $1 < a < 2$ and $1 < s < 3$ do not differ significantly from the plotted curves.

Fig. 10.— S_m - ν_m changes in the core. The lines and letters indicate different stages of the evolution of the shock, as described in section 4.1 and Table 5.

Fig. 11.— S_m - ν_m changes in C4 and C5. For each component, a dotted line shows possible tracks consistent with different stages of the evolution of the shock (the corresponding model parameters are given in Table 5). The dot-dashed line shows how the original fit for C5 must be changed to satisfy the observed trajectory of the component (plotted in Figure 13).

Fig. 12.— The observed trajectory of C5 in the plane of the sky. The dotted line represents the combined polynomial fits to the component's x and y offsets from the core. Open circles mark the locations on the trajectory which are equally spaced in time at an interval of 1 year.

Fig. 13.— The kinematic and shock-model b -parameters for C4 and C5. Different symbols show the b -parameters determined for the $\gamma = const$ (triangles) and $\gamma = \gamma_{\min}$ (circles) kinematic solutions. Solid lines represent the changes of the b -parameters of the components, as described in Table 5. Dot-dashed lines indicate the ranges of b -parameters for which a the turnover frequency can have a peak in time during the Compton-loss stage of the evolution of the shock.

Fig. 14.— Relative changes of the Doppler factor and magnetic field in the VLBI core, obtained by applying Königl jet model to the measured S_m and ν_m . The variations of all quantities are normalized to their respective values at the first epoch, $t_0 = 1981.5$. Open circles denote the changes of the particle density required for maintaining a constant Doppler factor. The dotted line shows the variations of the particle density, as represented by 5 exponential flares (the parameters of the flares are listed in the section “spectrum” of Table 7). The resulting variations of the Doppler factor (open squares) and magnetic field (filled triangles) are also shown, with lines representing linear fits to the respective quantity. The epochs of the flares are indicated in the bottom by the stars. For each flare, a segment indicates the relative increase of the particle density during the flare. The first and the last flares are not constrained by the data; the trapezia indicate the acceptable ranges of the locations and the amplitudes of these flares. The total 22 GHz flux density light curve (Teräsraanta 1998 and priv.comm.) is plotted for comparison. The light curve is scaled down by a factor of 100.

Fig. 15.— Application of the flare model to the observed variations of the 22 GHz flux density of the VLBI core in 3C 345. Filled triangles are the measured flux densities of the core. The solid line is the fit by the flare model. The parameters of the flares are listed in the section “light curve” of Table 7. If the current flare is similar to the flare in 1992, the dashed line should represent the expected evolution of the flux density in the core. Open circles show the changes in the total emission at 22 GHz (Teräsranta 1998 and priv.comm.). The flux densities of the core for the period 1994–1997 are taken from Leppänen (1995) and Ros et al. (1999).

Table 1: Multi frequency data sets.

(1)	(2)	(3)	(4)	(5)	(6)
τ_ν	t_{obs}	ν	S_{VLBI}	S_{tot}	Ref.
	1979.25	4.99	7.50 ± 0.41	...	1
1979.3	1979.44	10.70	8.53 ± 1.28	8.59 ± 0.14	1,9
	1980.52	10.70	10.48 ± 1.93	10.13 ± 0.10	1,9
1980.6	1980.73	4.99	7.40 ± 0.15	8.02 ± 0.05	1,9
	1981.09	10.70	12.83 ± 1.24	13.01 ± 0.60	1,9
	1981.25	22.30	13.87 ± 0.30	14.92 ± 0.77	1,10
	1981.63	4.99	9.89 ± 0.17	10.08 ± 0.05	1,9
1981.5	1981.68	2.30	6.27 ± 0.67	...	1
	1982.09	10.70	15.19 ± 0.53	15.34 ± 0.32	1,9
	1982.38	89.20	12.00 ± 6.40	13.47 ± 8.62	1,10
1982.4	1982.56	4.99	10.67 ± 0.30	11.35 ± 0.07	1,9
	1983.09	22.30	13.20 ± 0.90	15.01 ± 0.28	1,10
	1983.10	10.70	14.66 ± 1.06	14.67 ± 0.26	1,9
1983.4	1983.57	4.99	9.52 ± 0.87	11.44 ± 0.15	1,9
	1984.09	22.30	13.20 ± 0.64	13.87 ± 0.23	1,10
	1984.11	10.70	13.74 ± 0.84	14.12 ± 0.31	1,9
1984.2	1984.25	4.99	7.43 ± 0.38	12.80 ± 0.12	2,9
	1985.75	22.30	6.36 ± 0.18	10.90 ± 0.28	2,10
	1985.77	4.99	9.25 ± 0.24	11.52 ± 0.06	2,9
1985.8	1985.93	10.70	9.88 ± 0.72	11.44 ± 0.79	2,9

Table 1: (continued)

(1)	(2)	(3)	(4)	(5)	(6)
τ_ν	t_{obs}	ν	S_{VLBI}	S_{tot}	Ref.
	1986.90	4.99	10.01 ± 0.82	10.56 ± 0.08	2,9
	1987.15	10.70	9.47 ± 0.16	11.03 ± 0.48	2,9
1987.3	1987.42	22.30	3.93 ± 0.10	9.32 ± 0.21	2,10
	1988.16	22.30	5.07 ± 0.09	7.73 ± 0.18	2,10
	1988.17	10.70	8.70 ± 0.78	8.86 ± 0.52	2,9
	1988.18	4.99	7.84 ± 0.12	9.52 ± 0.09	2,9
1988.2	1988.21	100.00	3.20 ± 0.85	...	3
	1989.22	100.00	3.20 ± 0.52	...	3
	1989.25	22.30	5.98 ± 0.30	5.89 ± 0.21	7,9
	1989.26	10.70	7.53 ± 0.56	7.01 ± 0.33	7,8
1989.2	1989.28	4.99	7.85 ± 0.45	8.06 ± 0.06	4,8
	1990.16	10.70	3.14 ± 0.16	5.81 ± 0.03	6,8
	1990.18	4.99	6.50 ± 0.35	6.56 ± 0.06	4,8
	1990.42	22.30	3.01 ± 0.22	5.92 ± 0.20	6,9
1990.3	1990.49	43.20	7.88 ± 0.76	5.04 ± 0.45	5,8
	1991.68	43.20	22.70 ± 4.54	...	5
	1991.71	4.99	4.97 ± 0.82	5.24 ± 0.05	4,8
1991.7	1991.86	22.30	12.10 ± 0.72	12.36 ± 0.28	7,9
	1992.43	4.99	6.61 ± 0.74	6.43 ± 0.04	7,8
	1992.45	22.30	13.23 ± 2.04	11.97 ± 0.43	7,9
1992.5	1992.71	8.40	10.59 ± 4.08	10.35 ± 0.15	7,8

Table 1: (continued)

(1)	(2)	(3)	(4)	(5)	(6)
τ_ν	t_{obs}	ν	S_{VLBI}	S_{tot}	Ref.
	1993.70	4.99	6.42 ± 0.46	8.15 ± 0.06	7,8
	1993.72	22.30	6.14 ± 0.16	8.53 ± 0.31	7,9
1993.8	1993.88	8.40	8.48 ± 0.20	9.99 ± 0.19	7,8

Note. — 1 – multi frequency data set epoch; 2 – observation epoch; 3 – frequency, GHz ; 4 – VLBI flux density , Jy; 5 – total flux density, Jy; 6 – references for the VLBI and total flux density measurements (for the 10.7 and 43.2 GHz VLBI observations, the table gives the flux densities at 8 and 37 GHz respectively).

References. — 1 – Biretta et al. 1986; 2 – Zensus et al. 1995; 3 – Bååth et al. 1992; 4 – Unwin & Wehrle 1992; 5 – Krichbaum et al. 1993; 6 – Unwin et al. 1994; 7 – Lobanov 1996; 8 – Aller et al. 1996; 9 – Teräsranta et al. 1998.

Table 2: Spectral fits.

(1)	(2)	(3)	(4)	(5)	(6)	(7)	(8)	(9)	(10)
Name	τ_ν	N_ν	$\sigma_{S,N}$	S_{int}	S_m	ν_m	α_{fit}	γ_{min}	$L_{max}^{4-25 GHz} h^{-2}$
D	1979.3	2	6.1	81.8 ± 3.7	(4.7)	(10.5)	-0.1	(3.5)	$8.0 \cdot 10^{42}$
	1980.6	2	15.9	82.6 ± 3.2	(4.6)	(8.5)	-0.2	(3.5)	$8.0 \cdot 10^{42}$
	1981.5	4	8.5	164.9 ± 8.9	10.1 ± 5.8	14.9 ± 1.2	-0.1	(3.5)	$1.2 \cdot 10^{43}$
	1982.4	3	9.0	135.3 ± 7.5	7.4 ± 1.4	6.7 ± 0.6	-0.3	(3.5)	$1.3 \cdot 10^{43}$
	1983.4	3	6.8	113.1 ± 5.7	5.6 ± 1.5	10.1 ± 1.0	-0.2	(3.5)	$9.2 \cdot 10^{42}$
	1984.2	3	4.1	117.6 ± 6.0	6.8 ± 3.1	22.5 ± 1.1	-0.1	(3.5)	$7.9 \cdot 10^{42}$
	1985.8	3	7.7	71.3 ± 2.4	3.7 ± 0.7	12.1 ± 0.6	-0.2	(3.5)	$5.8 \cdot 10^{42}$
	1987.3	3	13.7	44.8 ± 1.3	2.3 ± 0.6	12.1 ± 1.6	-0.1	(3.5)	$3.7 \cdot 10^{42}$
	1988.2	4	9.5	33.8 ± 1.0	1.9 ± 0.6	13.2 ± 0.9	-0.1	(3.5)	$2.9 \cdot 10^{42}$
	1989.2	4	6.4	29.7 ± 1.2	1.4 ± 0.3	10.3 ± 4.3	-0.2	(3.5)	$2.5 \cdot 10^{42}$
	1990.3	4	5.4	31.9 ± 1.1	1.6 ± 0.6	15.6 ± 6.4	-0.1	(3.5)	$2.5 \cdot 10^{42}$
	1991.7	3	6.9	106.0 ± 4.1	7.3 ± 3.5	32.5 ± 6.8	-0.1	(3.5)	$6.3 \cdot 10^{42}$
	1992.5	3	9.9	195.6 ± 6.7	11.9 ± 4.3	24.0 ± 1.2	-0.1	(3.5)	$1.2 \cdot 10^{43}$
	1993.8	3	2.4	66.4 ± 3.0	4.0 ± 1.6	20.0 ± 1.8	-0.1	(3.5)	$4.4 \cdot 10^{42}$

Table 2: (continued)

(1)	(2)	(3)	(4)	(5)	(6)	(7)	(8)	(9)	(10)
Name	τ_ν	N_ν	$\sigma_{S,N}$	S_{int}	S_m	ν_m	α_{fit}	γ_{min}	$L_{\text{max}}^{4-25 \text{ GHz}} h^{-2}$
C5	1984.2	3	12.5	34.7 ± 2.3	4.9 ± 1.1	2.5 ± 0.4	-0.8	2.3	$1.2 \cdot 10^{43}$
	1985.8	3	6.8	51.2 ± 3.0	3.3 ± 0.3	6.0 ± 0.3	-0.6	3.3	$6.1 \cdot 10^{42}$
	1987.3	3	8.1	80.7 ± 5.1	5.1 ± 0.2	7.0 ± 0.6	-0.8	4.3	$5.4 \cdot 10^{42}$
	1988.2	4	7.5	98.0 ± 4.0	5.6 ± 0.5	7.5 ± 0.4	-0.7	5.0	$4.5 \cdot 10^{42}$
	1989.2	3	5.3	28.1 ± 1.6	4.7 ± 0.6	2.5 ± 1.4	-0.9	5.7	$1.7 \cdot 10^{42}$
	1990.3	3	5.4	26.8 ± 1.1	3.6 ± 0.1	2.5 ± 1.2	-0.9	6.0	$1.4 \cdot 10^{42}$
	1991.7	2	9.3	14.3 ± 1.2	(1.1)	(3.2)	-0.5	5.7	$6.6 \cdot 10^{41}$
	1992.5	3	12.3	9.2 ± 0.7	1.5 ± 0.3	2.2 ± 0.8	-0.9	5.0	$7.4 \cdot 10^{41}$
	1993.8	2	5.7	5.5 ± 0.6	(0.8)	(2.3)	-0.8	2.8	$1.4 \cdot 10^{42}$

Table 2: (continued)

(1)	(2)	(3)	(4)	(5)	(6)	(7)	(8)	(9)	(10)
Name	τ_ν	N_ν	$\sigma_{S,N}$	S_{int}	S_m	ν_m	α_{fit}	γ_{min}	$L_{\text{max}}^{4-25 \text{ GHz}} h^{-2}$
C4	1981.5	2	6.1	71.3 ± 4.4	(3.5)	(9.2)	-0.2	3.2	$7.4 \cdot 10^{42}$
	1982.4	2	6.7	162.7 ± 7.1	(8.0)	(10.0)	-0.2	4.2	$9.5 \cdot 10^{42}$
	1983.4	3	5.1	130.6 ± 6.4	7.5 ± 0.6	11.6 ± 0.4	-0.5	4.7	$5.6 \cdot 10^{42}$
	1984.2	2	5.4	113.2 ± 6.2	(5.6)	(14.1)	-0.2	4.4	$6.0 \cdot 10^{42}$
	1985.8	3	6.4	36.3 ± 3.0	1.9 ± 0.1	9.4 ± 0.6	-0.2	4.2	$2.3 \cdot 10^{42}$
	1987.3	2	10.9	22.1 ± 1.5	(3.1)	(2.5)	-0.8	5.5	$1.5 \cdot 10^{42}$
	1988.2	3	17.2	12.2 ± 0.8	0.8 ± 0.1	6.5 ± 1.4	-0.6	7.2	$3.1 \cdot 10^{41}$
	1989.2	2	3.4	43.3 ± 2.8	(3.0)	(5.9)	-0.8	9.6	$7.5 \cdot 10^{41}$
	1990.3	2	22.0	6.7 ± 1.4	(2.0)	(1.8)	-1.4	12.2	$1.3 \cdot 10^{41}$
	1991.7	2	19.3	8.0 ± 0.8	(0.8)	(2.8)	-0.6	14.9	$5.7 \cdot 10^{40}$
	1992.5	3	22.1	15.7 ± 1.2	1.6 ± 0.1	2.7 ± 1.6	-0.7	14.2	$1.3 \cdot 10^{41}$
	1993.8	2	5.7	12.4 ± 1.3	(0.7)	(5.2)	-0.1	9.8	$1.7 \cdot 10^{41}$

Table 2: (continued)

(1)	(2)	(3)	(4)	(5)	(6)	(7)	(8)	(9)	(10)
Name	τ_ν	N_ν	$\sigma_{S,N}$	S_{int}	S_m	ν_m	α_{fit}	γ_{min}	$L_{\text{max}}^{4-25\text{ GHz}} h^{-2}$
C3	1979.3	2	5.5	36.3 ± 3.2	(2.2)	(4.5)	-0.2	7.3	$9.3 \cdot 10^{41}$
	1980.6	2	5.8	19.9 ± 1.1	(3.2)	(2.3)	-1.0	6.4	$1.1 \cdot 10^{42}$
	1981.5	3	8.8	22.5 ± 1.3	2.4 ± 0.2	2.7 ± 0.3	-0.8	6.0	$1.1 \cdot 10^{42}$
	1983.4	2	12.9	13.1 ± 0.7	(2.0)	(2.4)	-0.9	5.6	$8.6 \cdot 10^{41}$
	1984.2	2	7.5	10.1 ± 0.6	(0.8)	(3.1)	-0.5	5.7	$4.9 \cdot 10^{41}$
	1985.8	2	29.5	6.2 ± 1.5	(0.8)	(0.5)	-0.5	6.2	$5.8 \cdot 10^{41}$
	1988.2	2	15.7	8.3 ± 1.0	(0.7)	(3.0)	-0.5	7.9	$2.1 \cdot 10^{41}$
	1989.2	2	6.9	17.1 ± 1.2	(1.0)	(16.8)	-0.1	8.9	$2.5 \cdot 10^{41}$
	1992.5	2	18.4	8.2 ± 1.2	(0.4)	(8.4)	-0.1	13.4	$5.8 \cdot 10^{40}$
	1993.8	2	14.1	3.1 ± 1.4	(0.3)	(2.5)	-0.6	15.7	$2.2 \cdot 10^{40}$

Table 2: (continued)

(1)	(2)	(3)	(4)	(5)	(6)	(7)	(8)	(9)	(10)
Name	τ_ν	N_ν	$\sigma_{S,N}$	S_{int}	S_m	ν_m	α_{fit}	γ_{min}	$L_{\text{max}}^{4-25\text{ GHz}} h^{-2}$
C2	1979.3	2	34.3	13.1 ± 0.9	(0.9)	(3.5)	-0.3	7.8	$3.1 \cdot 10^{41}$
	1980.6	2	12.2	15.0 ± 1.1	(0.8)	(5.4)	-0.1	8.2	$2.9 \cdot 10^{41}$
	1981.5	3	10.9	16.9 ± 1.0	(2.0)	(1.4)	-0.4	8.4	$4.0 \cdot 10^{41}$
	1984.2	2	33.1	12.5 ± 0.8	(0.7)	(9.4)	-0.2	9.1	$1.9 \cdot 10^{41}$
	1989.2	2	7.5	10.7 ± 1.2	(0.6)	(5.4)	-0.1	10.5	$1.3 \cdot 10^{41}$

Note. — The table columns are: 1 – component name; 2 – multi frequency data set epoch; 3 – number of frequencies available for spectral fit; 4 – mean fractional flux density error in a spectral dataset [%]; 5 – integrated 4–25 GHz flux [$\cdot 10^{-14}$ erg s $^{-1}$ cm $^{-2}$]; 6 – turnover flux density [Jy]; lower limits are given in brackets; 7 – turnover frequency [GHz]; upper limits are given in brackets; 8 – fitted spectral index; 9 – minimum Lorentz factor; 10 – upper limit for 4–25 GHz luminosity [erg s $^{-1}$].

Table 3: Luminosity evolution in parsec-scale features of 3C345

Component	$\log[L_{4-25\text{ GHz}}(t)]$	Comment
D	$43.360 - 0.091\tau$	1981–88
C5	$43.695 - 0.128\tau$	
C4	$43.517 - 0.182\tau$	
C3	$42.280 - 0.110\tau$	
C2	$41.568 - 0.045\tau$	

Note. — $\tau = t - 1979.0$ [years], where t is current epoch.

Table 4: Correlation between the component luminosity and kinematics

Component	$\log[L_{4-25\text{ GHz}}(R_{\text{app}})]$	$\log[L_{4-25\text{ GHz}}(R_j)]$ $\gamma = \text{const}$	$\log[L_{4-25\text{ GHz}}(R_j)]$ $\gamma = \gamma_{\text{min}}(t)$
C5	$43.548 - 0.326 R_{\text{app}}$	$43.323 - 0.654 R_j$	$43.534 - 0.668 R_j$
C4	$43.346 - 0.661 R_{\text{app}}$	$41.987 - 0.027 R_j$	$43.423 - 0.945 R_j$
C3	$42.756 - 0.286 R_{\text{app}}$	$41.221 - 0.018 R_j$	$42.609 - 0.567 R_j$
C2	$41.932 - 0.100 R_{\text{app}}$	$41.220 - 0.011 R_j$	$42.067 - 0.234 R_j$
All	$42.914 - 0.290 R_{\text{app}}$	$42.060 - 0.030 R_j$	$43.066 - 0.638 R_j$

Table 5: Component $S_m - \nu_m$ evolution in terms of shock-in-jet model

Period	ρ [$S_m \propto \nu_m^\rho$]	b [$\delta \propto R^b$]	ε [$\nu_m \propto R^\varepsilon$]	Stage
D:	$a = 1, s = 1.2$			
1981.5–82.4	0.4	–0.5	–1.1	Synchrotron
		–0.2	–1.2	Adiabatic
1984.2–85.8	1.0	–0.9	–1.4	Synchrotron
1985.8–89.3	2.3	–5.8	–4.6	Adiabatic
1990.2–91.8	3.2	5.0	3.2	Compton
1991.8–92.5	–0.7	–0.1	–0.8	Synchrotron
1992.5–93.8	2.3	–5.8	–4.6	Adiabatic
C5:	$a = 1, s = 2.4$			
1985.8–88.3	5.1	2.0	1.0	Compton
1988.3–89.2	0.0	0.0	–1.0	Synchrotron
1989.2–92.5	1.8	–2.6	–3.1	Adiabatic
	(0.8)	(–0.2)	(–1.5)	Adiabatic ¹
C4:	$a = 1, s = 2.4$			
1983.4–88.2	2.8	–9.7	–7.8	Synchrotron
1988.2–92.5	–0.9	0.8	–0.8	Adiabatic

¹ used for the model described in section 4.2.4

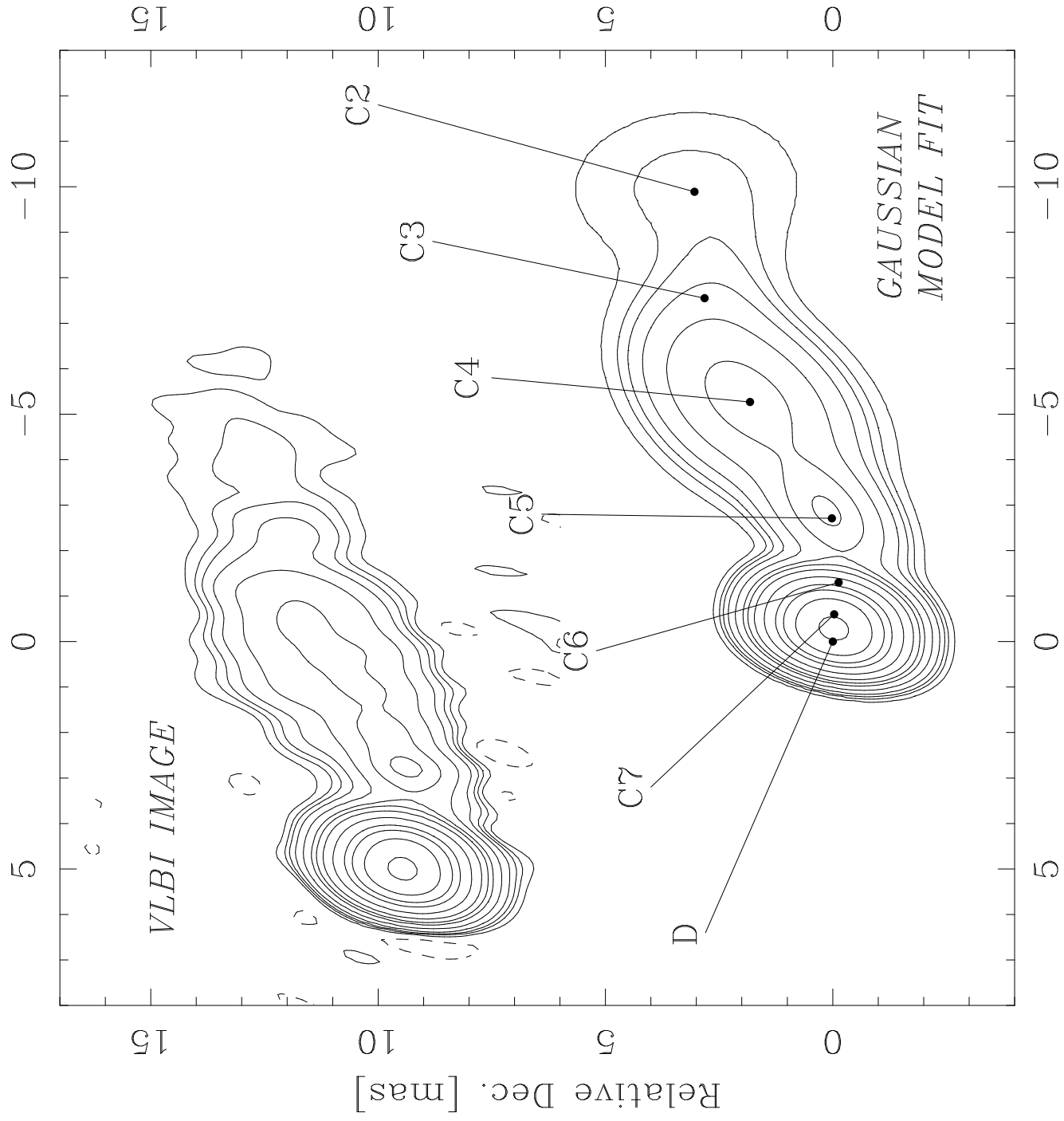
Table 6: Kinematics of C5 in the rest frame

$t_1 - t_2$ [years]	R_2/R_1	ΔR [pc]	R_1 [pc]	ΔR [pc]	R_1 [pc]
		($\delta_{01} = 1.05$)		($\delta_{02} = 2.80$)	
1985.8–88.2	1.1	4.2	29.3	6.1	42.0
1988.2–89.2	2.3	5.6	4.4	3.9	3.0
1989.2–92.5	1.6	8.3	13.4	14.5	23.2

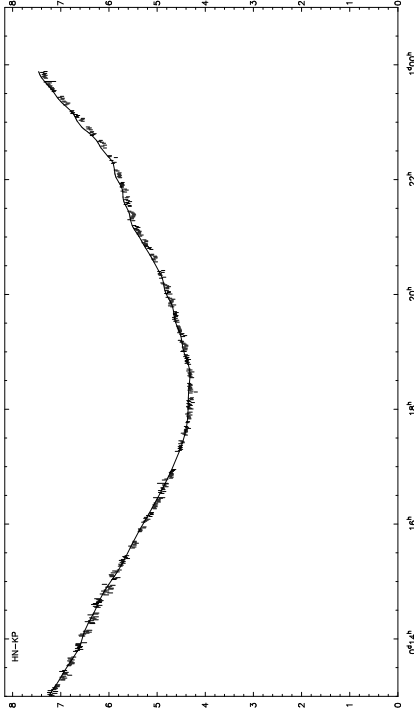
Table 7: Parameters of the flares in 3C 345

Flare	Spectrum			Light Curve		
	t_{flare}	N_{rel}	τ_{flare}	t_{flare}	N_{rel}	τ_{flare}
1	(1981.4)	$(1.0 \cdot 10^3)$	(0.5)	1981.4	$1.2 \cdot 10^4$	0.4
2	1984.6	$1.5 \cdot 10^3$	0.3	1984.2	$1.5 \cdot 10^4$	0.3
3	1987.8	$3.3 \cdot 10^1$	0.2	1986.6	$7.3 \cdot 10^1$	0.2
4	1992.0	$1.8 \cdot 10^3$	0.4	1991.7	$3.0 \cdot 10^4$	0.4
5	(1995.2)	$(1.8 \cdot 10^3)$	(0.4)	1995.2	$5.0 \cdot 10^2$	0.2
6				(1999.4)	$(3.0 \cdot 10^4)$	(0.4)

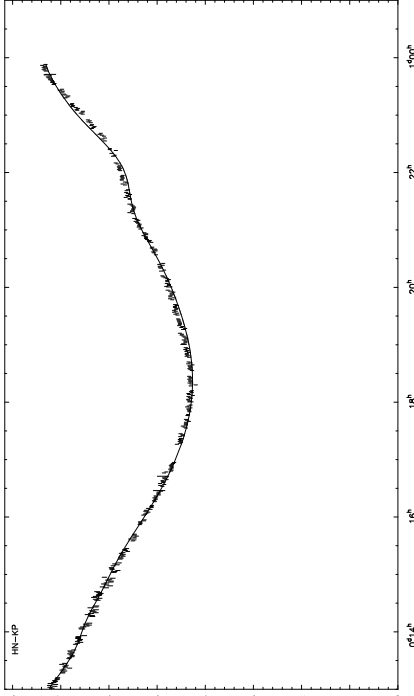
Note. — t_{flare} – epoch of the flare; N_{rel} – relative density increase; τ_{flare} – duration of the flare [yrs]. Bracketed values refer to the fits which are insufficiently constrained by the data.



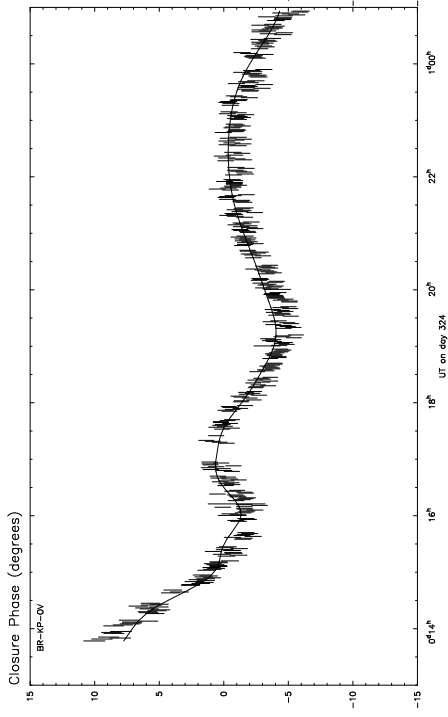
3C345 8.405 GHz 1993.89
Amplitude (Jy)



3C345 8.405 GHz 1993.89
Amplitude (Jy)



3C345 8.405 GHz 1993.89
Closure Phase (degrees)



3C345 8.405 GHz 1993.89
Closure Phase (degrees)

